Magnetic excitation spectrum and Hamiltonian of the quantum spin chain compound BaCuTe2O6

A. Samartzis, S. Chillal, H. O. Jeschke, D. J. Voneshen, Z. Lu, A. T. M. N. Islam, and B. Lake

Published version information

Citation: A Samartzis et al. Magnetic excitation spectrum and Hamiltonian of the quantum spin chain compound BaCuTe2O6. Phys Rev B 107, no. 18 (2023): 184435

DOI: 10.1103/PhysRevB.107.184435

Magnetic excitation spectrum and Hamiltonian of the quantum spin chain compound $BaCuTe_2O_6$

A. Samartzis,[1,2] S. Chillal,[1] H. O. Jeschke,[3,*] D. J. Voneshen,[4,5] Z. Lu,[1,6] A. T. M. N. Islam,[1] and B. Lake[1,2,†]

[1]*Helmholtz-Zentrum Berlin für Materialien und Energie GmbH, Hahn-Meitner Platz 1, D-14109 Berlin, Germany*

[2]*Institut für Festkörperphysik, Technische Universität Berlin, Hardenbergstraße 36, D-10623 Berlin, Germany*

[3]*Research Institute for Interdisciplinary Science, Okayama University, Okayama 700-8530, Japan*

[4]*ISIS pulsed neutron and muon source, STFC Rutherford Appleton Laboratory, Oxfordshire OX11 0QX, United Kingdom*

[5]*Department of Physics, Royal Holloway University of London, Egham, TW20 0EX, United Kingdom*

[6]*School of Computing, Engineering and The Built Environment, Edinburgh Napier University, Edinburgh EH10 5DT, United Kingdom*

(Received 8 February 2023; revised 4 May 2023; accepted 5 May 2023; published 18 May 2023)

The magnetic excitation spectrum and Hamiltonian of the quantum magnet $BaCuTe_2O_6$ is studied by inelastic neutron scattering (INS) and density functional theory (DFT). INS on powder and single crystal samples reveals overlapping spinon continua—the spectrum of an antiferromagnetic spin-1/2 spin chain—due to equivalent chains running along the a, b, and c directions. Long-range magnetic order onsets below $T_N = 6.3$ K due to interchain interactions, and is accompanied by the emergence of sharp spin-wave excitations, which replace the continua at low energies. The spin-wave spectrum is highly complex and was successfully modelled achieving excellent agreement with the data. The extracted interactions reveal an intrachain interaction, $J_3 = 2.9$ meV, while the antiferromagnetic hyperkagome interaction J_2 is the subleading interaction responsible for coupling the chains together in a frustrated way. DFT calculations reveal a similar picture for $BaCuTe_2O_6$ of dominant J_3 and subleading J_2 antiferromagnetic interactions and also indicate a high sensitivity of the interactions to small changes of structure, which could explain the very different Hamiltonians observed in the sister compounds $SrCuTe_2O_6$ and $PbCuTe_2O_6$.

DOI: 10.1103/PhysRevB.107.184435

I. INTRODUCTION

The compounds $ACuTe_2O_6$ ($A = Sr^{2+}$, Pb^{2+}, Ba^{2+}) form a fascinating family of materials. Their properties include quantum magnetism, spin liquid behavior, ferroelectricity, and magnetoelectricity. The magnetic properties arise from the Cu^{2+} ions, which have quantum spin-1/2 and are coupled by antiferromagnetic (AFM) interactions into chain and triangular structures. Meanwhile, the dielectric properties probably arise from the lone pair of electrons on the Te^{4+} and Pb^{2+} ions. The compounds form in the cubic space group $P4_132$ (#213) where all the Cu^{2+} ions are equivalent and occupy the single 12*d* Wyckoff site. The Cu^{2+} ions are coupled by a combination of one-dimensional (1D) and frustrated magnetic exchange interactions. As shown by Fig. 1, the first-neighbor interaction J_1 couples them into isolated triangles, the second-neighbor interaction J_2 couples them into a three-dimensional (3D) network of corner-sharing triangles known as the highly frustrated hyperkagome lattice and the third-neighbor interaction, J_3 couples them into chains with equivalent chains parallel to the a, b, and c axes due to the cubic symmetry. In addition, there are further-neighbor interactions such as J_4, which also give rise to spin chains along the body diagonals and J_6, which couples together the parallel chains formed by the J_3 interaction.

Behavior consistent with a quantum spin liquid was found in $PbCuTe_2O_6$. No indication of long-range magnetic order or spin freezing was found using a variety of experimental techniques even down to 20 mK [1–5]. Instead, both nuclear magnetic resonance and muon spin resonance measurements suggested a non-spin-singlet ground state with persistent spin fluctuations [2], while inelastic neutron scattering showed broad diffuse excitations inconsistent with the spin waves of a conventional magnet. Density functional theory calculations showed that the hyperkagome interaction J_2 is antiferromagnetic and strongest giving rise to strong magnetic frustration [1,3] while the J_1 interaction was found to have similar strength [3], leading to the novel hyper-hyperkagome lattice—a member of the distorted windmill lattice family [6,7]. Pseudo-Fermion functional renormalization group calculations based on these interactions confirm the absence of magnetic order and reproduce the observed magnetic structure factor. Further theoretical works using projective symmetry group analysis also suggest that $PbCuTe_2O_6$ could host quantum spin liquid states [8,9]. More recently, interest has turned to a 1 K transition found in the single crystal samples, which has been identified as a transition to ferroelectric order possibility related to the lone pairs on both the Pb^{2+} and Te^{4+} ions [4]. Interestingly, no long-range magnetic order was found so far to occur at this transition [4] and, furthermore, the transition is suppressed in powder samples because it is energetically unfavorable in small crystallites [5].

The behavior of $SrCuTe_2O_6$ is very different from $PbCuTe_2O_6$. In this compound the unfrustrated J_3 interaction

*jeschke@okayama-u.ac.jp

†bella.lake@helmholtz-berlin.de

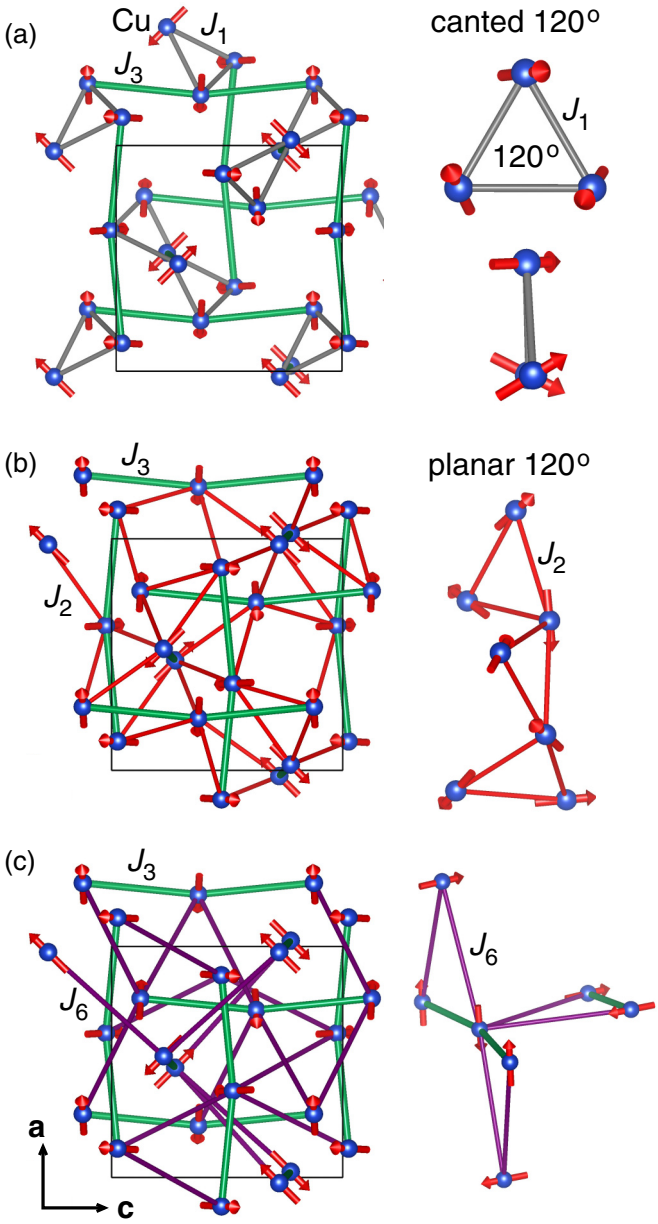

FIG. 1. Visualization of the crystal structure of the ACuTe$_2$O$_6$ family showing only the Cu^{2+} ions, which are represented by blue spheres. The crystal symmetry is cubic and the structure is viewed perpendicular to the b axis, where the black lines indicate a unit cell. The colored lines indicate the different magnetic exchange interactions. The red arrows give the magnetic structure specific to BaCuTe$_2$O$_6$ [10]. (a) Includes the first J_1 (grey line) and third J_3 (green line) nearest-neighbor interactions. Note that J_3 produces equivalent chains parallel to the a, b, and c axes due to the cubic crystal symmetry, while J_1 produces isolated triangles. (b) Includes the second J_2 hyperkagome interaction given by the red line and the third J_3 interaction (green line). (c) Includes the J_6 interaction (purple line) which creates chains parallel to the body diagonals and the J_3 interaction (green line). On the right-hand side of panels (a), (b), and (c), the triangles formed by J_1, J_2, and J_3&J_6 are presented respectively. This figure was produced using the VESTA software [11].

is dominant and antiferromagnetic giving rise to three equivalent spin chains parallel to the a, b, and c axes. Evidence for this comes from broad peaks due to short-range order in the DC susceptibility and heat capacity [12–16]. Furthermore, inelastic neutron scattering finds that the excitations form a spinon continuum characteristic of the spin-1/2 Heisenberg antiferromagnetic chain [17]. Physical properties measurements also reveal two transitions to long-range magnetic order and a complex phase diagram as a function of magnetic field and temperature [12–16]. Furthermore, measurements of the dielectric properties reveal magnetoelectric behavior [13,14]. The long-range magnetic order in the ground state was studied by neutron diffraction and the magnetic structure is characterized by antiferromagnetic order along the J_3 chains and planar 120° order around the J_1 isolated triangles ($1 \times \Gamma_1^1$ irreducible representation) [15,16]. Since long-range magnetic order is not possible in a one-dimensional magnet [18], there must be additional magnetic interactions, which couple the chains together. Several density functional theory calculations were performed to calculate the interactions in SrCuTe$_2$O$_6$, which revealed that the strongest interchain interaction is the hyperkagome interaction J_2, which was initially found to be antiferromagnetic (AFM) [12,13] but later found to be ferromagnetic (FM) [19] along with a smaller AFM J_6 interaction [12,19]. The interchain interactions were also investigated by inelastic neutron scattering. By fitting the low-energy magnetic spectrum at low temperatures to spin-wave theory, Chillal *et al.* [17] showed that the FM J_2/AFM J_6 model is compatible with the data while an AFM J_1 also explains the spectrum.

The newest member of the ACuTe$_2$O$_6$ family is BaCuTe$_2$O$_6$. As for SrCuTe$_2$O$_6$, the unfrustrated J_3 interaction is also dominant and antiferromagnetic in BaCuTe$_2$O$_6$, giving rise to spin chains parallel to the a, b, and c axes. The intrachain interaction was found to have strength $J_3 = 2.93 - 3.19$ meV from DC susceptibility and heat capacity measurements [10,19]. This was confirmed by inelastic neutron scattering measurements, which observed the characteristic spinon continuum expected for a spin-1/2 Heisenberg antiferromagnetic chain, allowing comparison to theory, which yielded $J_3 = 2.90$ meV [10]. Long-range antiferromagnetic order occurs at the much lower temperature of $T_N = 6.1 - 6.3$ K [10,19] revealing the presence of weak interchain interactions. The magnetic structure was found to follow the $2 \times \Gamma_2^1$ irreducible representation [10]. It is illustrated by the red arrows along with the exchange interactions J_1, J_2, J_3, and J_6 in Fig. 1. As for SrCuTe$_2$O$_6$, the order is antiferromagnetic along the chains formed by J_3; however, there is canted 120° order about the isolated J_1 triangles rather than the planar 120° order of SrCuTe$_2$O$_6$. Furthermore, there is planar 120° order around the triangles of the hyperkagome lattice formed by J_2 (rather that canted 120° order). This suggests that an antiferromagnetic J_2 interaction is primarily responsible for coupling the J_3 chains and gives rise to the long-range magnetic order. Recent DFT calculations support this view, they predict that the chain interaction is $J_3 = 2.93$ meV, while $J_1 = 0.0$ meV and the interchain coupling is due to an AFM $J_2 = 0.43$ meV. They also predict an AFM $J_6 = 0.17$ meV while all other interactions are negligible [19].

In this paper we determine the magnetic exchange interactions of $BaCuTe_2O_6$ using two independent methods. We extract the interactions from the magnetic excitation spectrum observed at low temperatures and energies using inelastic neutron scattering (INS). We also perform density functional theory (DFT) calculations to estimate the interactions based on the crystal structure. The results are compared to those of $SrCuTe_2O_6$ and $PbCuTe_2O_6$.

II. MAGNETIC EXCITATION SPECTRUM

A. Experimental Details

Powder and single crystal samples of $BaCuTe_2O_6$ were synthesized and characterized at the Core Laboratory Quantum Materials, Helmholtz-Zentrum Berlin für Materialien und Energie, Germany. Further details can be found in Ref. [10].

The spin dynamics of $BaCuTe_2O_6$ were studied by inelastic neutron scattering (INS). Data for both powder and single crystal samples were collected on the LET, cold neutron multi-chopper Time-of-Flight spectrometer operating at Target Station 2 of the ISIS facility, Rutherford Appleton Laboratory, UK [21,22]. The samples were cooled using an orange cryostat and data were measured at $T = 2$ K and 8 K. The spectrum of the powder sample [mass 10.1(4) g] was collected simultaneously at five independent incident energies $E_i = 14.1$, 4.88, 2.45, 1.47, and 0.978 meV with corresponding elastic energy resolutions, $\Delta E_i = 0.697$, 0.144, 0.053, 0.025, and 0.014 meV for a total current of 240 μA and 310 μA at low and high temperatures, respectively. The single crystal sample consisted of three co-aligned crystals [total mass 4.80(1) g] oriented with the $[1, -1, 0]$ crystallographic direction vertical. The crystals were wrapped in Al foil and attached to an Al sample holder using Al wire. This sample was measured at $T = 2$ K and $T = 8$ K with incident energies, $E_i = 13.75$, 7.6, 4.81, 3.32, and 2.43 meV and corresponding elastic energy resolutions, $\Delta E_i = 0.782$, 0.333, 0.175, 0.105, and 0.068 meV. During the measurements the crystals were rotated about their vertical axis over an angular range of 159° in steps of 0.5° or 1° for a current of 8 μA per step. Data processing and visualization were carried out using the Horace software [23].

Further INS measurements were performed to provide information about the low-energy magnetic excitations below the transition temperature. The coaligned system of $BaCuTe_2O_6$ single crystals was measured again on the single detector, Triple-Axis-Spectrometer FLEXX, at Helmholtz-Zentrum Berlin für Materialien und Energie, Germany [24]. Data were collected at $T = 2$ K, using an orange cryostat. The wavevector of the scattered neutrons was fixed to $k_f = 1.3$ Å^{-1}, which provided an elastic energy resolution of $\Delta E = 0.12$ meV, while the monochromator was used in the horizontally and vertically focused mode to optimize intensity. Data were collected by scanning the energy with step size 0.05 meV, for fixed wavevectors along the $[1, 1, L]$, $[0, 0, L]$, and $[H, H, 1]$ directions with values of H and L taken at intervals of 0.1 r.l.u. or smaller, measuring for ≈3.54 min per step. In addition, Q scans at constant energy along the $[1, 1, L]$ and $[H, H, 1]$ directions were performed for a Q step of 0.05 r.l.u. for several fixed energies with the same counting time. The visualization of the data was achieved using the software package Spec1D in Matlab.

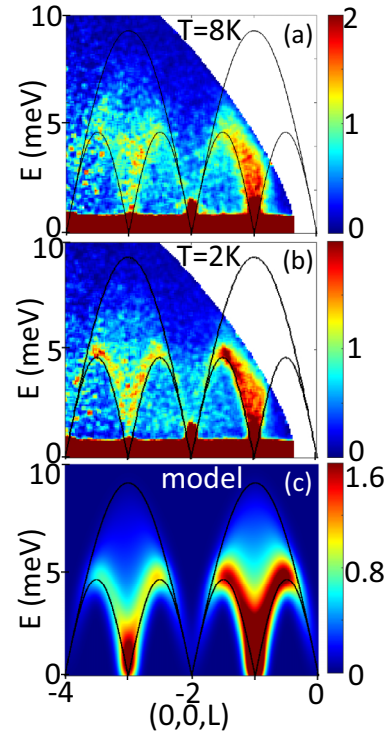

FIG. 2. High-energy inelastic neutron scattering measured on the single crystal sample of $BaCuTe_2O_6$ compared to the theoretical spinon continuum. The data were collected on the LET spectrometer using an incident neutron energy of $E_i = 13.75$ meV. The spectra are plotted as a function of energy and wavevector transfer along $[0, 0, L]$ for (a) $T = 8$ K ($> T_N = 6.3$ K) and (b) $T = 2$ K ($\ll T_N = 6.3$ K) respectively. They have been integrated by ±0.2 r.l.u. over both the $[H, H, 0]$ and $[K, -K, 0]$ directions and no background has been subtracted. (c) Dynamical structure factor calculated via the algebraic Bethe-Ansatz for $J_3 = 2.90(6)$ meV [20]. The magnetic form factor of the Cu^{2+} ion was also included in the calculations and the data have been convolved with a Gaussian of width 0.78 meV to reproduce the effect of the energy resolution. The black lines plotted over the data and simulation represent the upper and lower boundaries of the spinon continuum.

The magnetic Hamiltonian of $BaCuTe_2O_6$, was simulated using linear spin-wave theory within the Matlab package, SpinW [25] and compared to the data at low energies and temperatures to obtain the exchange interactions.

B. Results

Figure 2 shows the full magnetic spectrum from the single crystal sample plotted as a function of energy up to 10 meV and wavevector along the direction of one set of chains due to the J_3 interaction. The data were measured with an incident energy of 13.75 meV on the LET spectrometer just above the Néel temperature at 8 K($> T_N = 6.3$ K) [Fig. 2(a)] and well below it at 2 K($\ll T_N$) [Fig. 2(b)]. Only subtle changes are observed with the decrease in temperature at most energy scales. As discussed in Ref. [10] the spectrum is typical of a spin-1/2, Heisenberg, antiferromagnetic chain showing a spinon

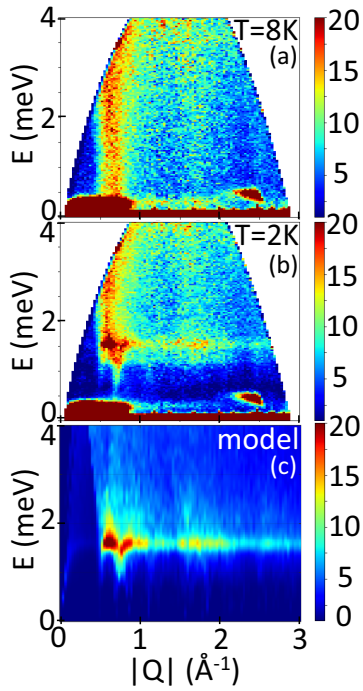

FIG. 3. Low-energy powder inelastic neutron scattering spectrum displayed as a function of energy and wavevector transfer. The data were measured using the LET spectrometer at (a) $T = 8$ K ($> T_N = 6.3$ K) and (b) $T = 2$ K ($\ll T_N = 6.3$ K) with an incident energy of $E_i = 4.88$ meV and energy resolution $\Delta E_i = 0.144$ meV. No background has been subtracted from the data. Note that the data below 0.5 meV are unreliable showing several spurious features. (c) shows the powder spectrum simulated by spin-wave theory for $J_3' = \pi J_3/2$ where $J_3 = 2.90$ meV, $J_2 = 0.30$ meV, $J_1 = 0.05$ meV, and $J_6 = 0.035$ meV. The magnetic form factor of the Cu^{2+} ion was also included. The simulations were convolved over energy by a Gaussian function with a full-width-at-half-maximum (FWHM) of 0.144 meV to reproduce the broadening due to the instrumental resolution.

continuum extending from a lower boundary given by the des Cloizeaux-Pearson expression $(\pi \times J_3/2)|\sin(\pi L)|$ to an upper boundary given by $(\pi \times J_3)|\sin(\pi L/2)|$ [26]. This allowed the value of the intrachain interaction, $J_3 = 2.90$ meV, to be extracted [10]. Figure 2(c) shows the theoretical spinon continuum simulated for this value of J_3 for comparison with the data.

Differences in the spectrum above and below T_N are most pronounced at low energies. Figure 3 presents the low-energy INS data collected on the LET spectrometer for the powder sample at 8 K [Fig. 3(a)] and 2 K [Fig. 3(b)] plotted as a function of energy and wavevector. At 8 K, there are streaks of scattering at the wavevectors 0.5 and 1.5 Å^{-1}, which are due to the spinon continuum that comes down to low energies at (0,0,1) and (0,0,3) respectively. Note that these minima occur at odd-integer rather than half-odd-integer values of L because each chain has two Cu^{2+} ions per unit cell. These are the same features observed in the high-energy single crystal data shown in Fig. 2. Below T_N the low-energy spectrum is very different, a flat band appears at ≈1.6 meV and at lower energies new weak streaks appear at the wavevectors 0.5, 0.7, and 1.15 Å^{-1}, which correspond to the magnetic Bragg peaks (0,0,1), (1,1,0), and (0,1,2)/(1,1,2) observed in neutron diffraction [10].

In order to learn more about the low-energy spin dynamics of $BaCuTe_2O_6$, further INS data were collected from the single crystal sample using lower incident energies on the LET spectrometer. Figure 4 presents the spectrum collected for an incident energy of $E_i = 4.81$ meV plotted as a function of energy and wavevector for selected high symmetry directions. Above T_N at 8 K, strong magnetic signal is observed at odd integer values of H and L due to the spinon continuum; however, at 2 K the signal below 2 meV is again significantly modified with a new dispersionless band at ≈1.6 meV, and the intensities at lower energies are dramatically altered.

These changes can also be observed in the constant energy slices plotted in Fig. 5. At 8 K [Figs. 5(a) to 5(d)] two sets of perpendicular streaks are observed. The streaks parallel to $[H, H, 0]$, which are strongest for odd H, are due to the J_3 chains parallel to the **c**-axis. These chains are effectively decoupled above T_N so that the dispersion perpendicular to these chains is negligible. Likewise, the streaks parallel to $[0, 0, L]$ are due to the chains along the a and b directions. Below T_N [Figs. 5(e) to 5(h)] the excitations have clearly become dispersive. At the lowest energies, the streaks are replaced by dots suggesting spin-waves dispersing upwards from integer values of H and L. Above ≈1.2 meV the streaks are again visible; however, they appear sharper than at 8 K and close observation shows them to be in fact double streaks, providing further evidence that these excitations are spin waves.

The results from the single crystal measurement on the FLEXX spectrometer are similar to the LET results. Figure 6 shows the data at 2 K as a function of energy and wavevector along various directions. A corresponding measurement above T_N was not performed on this spectrometer.

In summary, while we can think of the chains due to the J_3 interaction as being essentially decoupled above T_N resulting in a spinon continuum in $BaCuTe_2O_6$, at lower temperatures the interchain coupling gives rise to long-range magnetic order and spin-wave excitations at low energies. The higher-energy spinon excitations are, however, almost unchanged by the transition. While the boundary between the spinon and spin-wave regimes is not sharp, the biggest temperature changes occur below $E \approx 1.6$ meV, which is the top of the interchain spin-wave dispersion at low temperatures (see Figs. 3, 4, and 6) identifying this as the spin-wave bandwidth. Above T_N this dispersion is gone implying that the spin waves (which have quantum spin number $S = 1$) have "deconfined" into pairs of spinons (which have quantum spin number $S = 1/2$). In contrast, above $E \approx 2.0$ meV the excitations are broad and show almost no changes with temperature suggesting that this is the spinon regime. The intermediate energy regime ($1.6 < E < 2.0$ meV) is a crossover regime where the excitations can be described as broadened spin waves or partially confined spinons.

Such confinement of the spinon excitations into spin waves at low energies and temperatures due to the interchain coupling was observed previously and studied extensively in the spin-chain compound $KCuF_3$ [27–29] and was also found in the sister compound $SrCuTe_2O_6$ [17], which is isostructural to $BaCuTe_2O_6$.

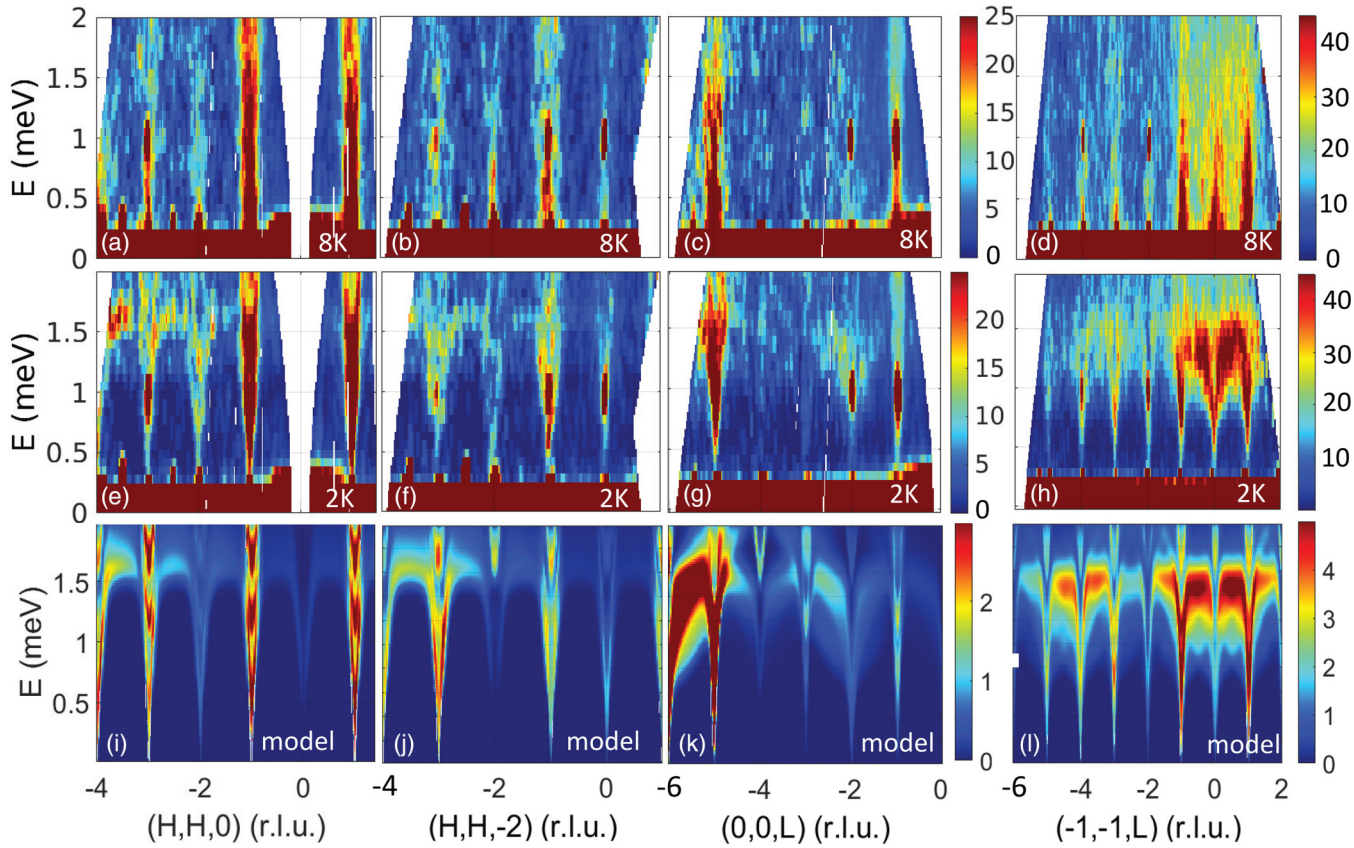

FIG. 4. Low-energy inelastic neutron scattering data measured on the single crystal sample and plotted as a function of energy and selected wavevector transfers. The data were collected on the LET spectrometer using an incident neutron energy of $E_i = 4.81$ meV. They are integrated by ± 0.1 r.l.u. over both the vertical, out-of-plane scattering direction $[K, -K, 0]$ and the horizontal direction perpendicular to the slice. (a), (b), (c), and (d) show the spectra along $[H, H, 0]$, $[H, H, -2]$, $[0, 0, L]$, and $[-1, -1, L]$ at $T = 8$ K, while (e)–(h) show the spectra below T_N at $T = 2$ K for the same directions. (i)–(l) show the corresponding dynamical structure factor calculated by linear spin-wave theory for interaction values of $J_3' = \pi J_3/2$ where $J_3 = 2.90$ meV, $J_2 = 0.30$ meV, $J_1 = 0.05$ meV, and $J_6 = 0.035$ meV, which is integrated over the same wavevector ranges as the data. The simulations were convolved over energy by a Gaussian function with FWHM of 0.175 meV to reproduce the broadening due to the instrumental resolution. The magnetic form factor of the Cu^{2+} ion was also included.

C. Analysis

Because we observe spin-wave excitations at low energies and temperatures in $BaCuTe_2O_6$, the low-energy INS data can be analyzed using linear spin-wave theory to extract the interchain exchange interactions. The steepest spin-wave dispersion along the chain at low energies merges with the lower boundary of the spinon continuum at higher energies given by the des Cloizeaux-Pearson expression $(\pi \times J_3/2)|\sin(\pi H)|$ [26]. Therefore, in order to model the dispersion along the chains using spin-wave theory, the renormalized intrachain exchange constant $J_3' = \pi \times J_3/2$ should be used. A consistent value of $2.84 < J_3 < 3.19$ meV has already been established in the literature from DC susceptibility, heat capacity, inelastic neutron scattering, and DFT [10,19]. Here we use $J_3 = 2.90$ meV derived by comparing our high-energy INS data to the spectrum of the theoretical spinon continuum (Fig. 2) [10], which gives us the value $J_3' = 4.56$ meV.

The spin-wave simulations for $BaCuTe_2O_6$ were calculated using the spinW program [25] with the intrachain coupling fixed at $J_3' = 4.56$ meV. The interchain interactions J_1, J_2, and J_6 were included and all the interactions were assumed to be isotropic or Heisenberg, which is usually a good approximation for Cu^{2+} ions. The neutron scattering structure factor was simulated for a very wide range of combinations of both ferromagnetic and antiferromagnetic values of the intrachain couplings. In all cases a complex multibranch spin-wave spectrum was found. Many of the combinations could be instantly rejected because they were incompatible with the known magnetic structure of $BaCuTe_2O_6$ [10]. The simulations from the remaining combinations were compared to various low-energy cuts and slices at 2 K collected on the LET and FLEXX spectrometers such as those shown in Figs. 4–6. A detailed visual comparison was performed of the data and simulation taking into account both the dispersion energies and intensities to judge if there was a match. The ranges of the exchange interactions found to be compatible with the data are described in Table I and lie within the rectangular area in Fig. 7.

We found that it is essential to have a finite and antiferromagnetic J_2 to explain the data. This is to be expected because of the 120° magnetic order around each corner-sharing triangle formed by this interaction. At the same time we found the values of J_1 and J_2 to be highly coupled. J_2 can take values in the range $0.17 < J_2 < 0.44$ meV. For a given J_2, J_1 was

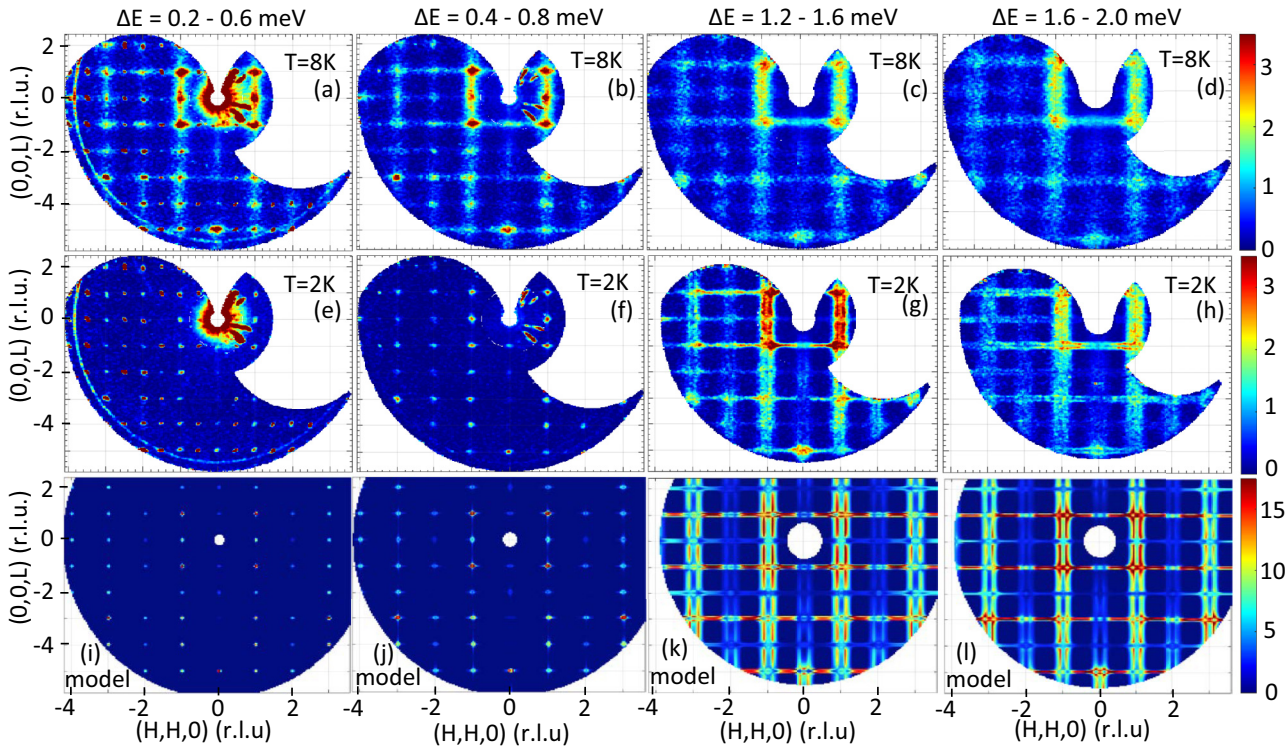

FIG. 5. Low-energy inelastic neutron scattering data measured on the single crystal sample plotted as a function of wavevector transfer in the $[H, H, L]$-plane for various energy integration ranges, which are given in the titles. The data were measured using the LET spectrometer at (a)–(d) $T = 8$ K and (e)–(h) $T = 2$ K using an incident energy of $E_i = 4.81$ meV. The data were integrated over wavevector in the vertical out-of-plane direction $[K, -K, 0]$ by ± 0.2 r.l.u. No background subtraction has been performed and only a weak smoothing is implemented. The strong non-symmetric features at low energies and wavevector are spurious background from the instrument. (i)–(l) show the corresponding single crystal spectrum simulated by spin-wave theory for $J_3' = \pi J_3/2$ where $J_3 = 2.90$ meV, $J_2 = 0.30$ meV, $J_1 = 0.05$ meV, and $J_6 = 0.035$ meV and integrated over the same wavevector and energy ranges as the data. The simulations were convolved over energy by a Gaussian function with FWHM of 0.175 meV to reproduce the broadening due to the effects of instrumental resolution. The magnetic form factor of the Cu^{2+} ion was also included.

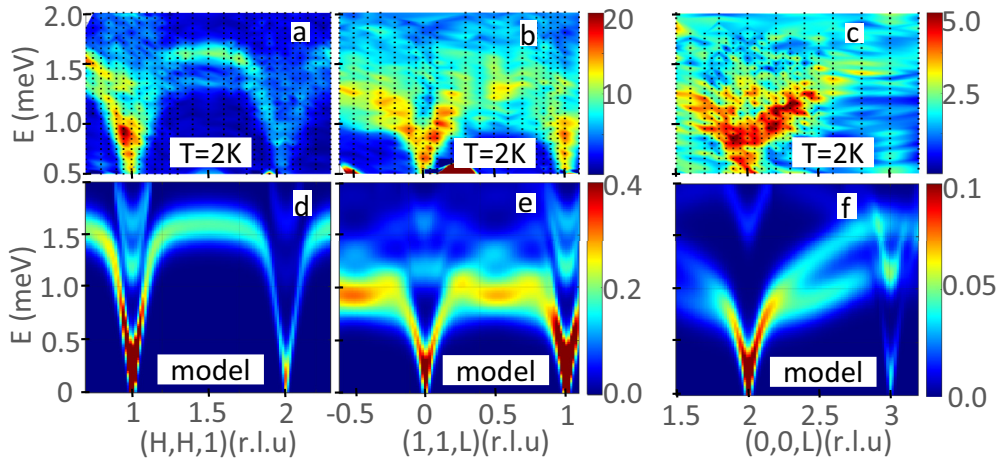

FIG. 6. Single crystal inelastic neutron scattering spectra as a function of energy and wavevector transfer along the (a) $[H, H, 1]$, (b) $[1, 1, L]$, and (c) $[0, 0, L]$ directions. The data were measured on the FLEXX spectrometer at $T = 2$ K ($< T_N = 6.3$ K). No background has been subtracted. (d)–(f) show the corresponding single crystal spectra simulated by spin-wave theory for $J_3' = \pi J_3/2$ where $J_3 = 2.90$ meV, $J_2 = 0.30$ meV, $J_1 = 0.05$ meV, and $J_6 = 0.035$ meV. The wavevector resolution broadening was included by taking the Gaussian weighted average over the expected resolution widths in the directions out-of-plane ($[K, -K, 0]$) and in-plane perpendicular to each slice by 0.1 $Å^{-1}$ and 0.02 $Å^{-1}$ respectively. The simulations were also convolved over energy by a Gaussian function of width 0.3 meV to mimic the broadening due to effects such as the instrumental energy resolution.

TABLE I. Allowed ranges of the exchange interaction of $BaCuTe_2O_6$ obtained by comparison of the INS spectrum to spin-wave theory. The units are meV.

J	Allowed values	Examples			
J_3	$J_3 = 2.90$ $J_3' = \pi J_3/2 = 4.56$	2.90	2.90	2.90	2.90
J_2	$0.17 < J_2 < 0.44$	0.17	0.27	0.30	0.44
J_1	$J_1 < 2J_2 - 0.52$ & $J_1 > 2J_2 - 0.56$	−0.20	0.00	0.06	0.34
J_6				$J_6 > -0.12$ & $J_6 < 0.18$	

found to lie within the range $2 \times J_2 - 0.56 < J_1 < 2 \times J_2 - 0.52$ meV. For the smallest value of $J_2 = 0.17$ meV, J_1 is ferromagnetic with size –0.20 meV, while for the largest value of $J_2 = 0.44$ meV, J_1 is antiferromagnetic of size 0.34 meV. The factor of two in the relation between J_2 and J_1 can be understood to arise from the fact that there are twice as many J_2 bonds as J_1 bonds so a two-times larger change in J_1 is needed to influence the spectrum. Finally J_6 was found to have very little effect on the excitations and could take either ferromagnetic values or antiferromagnetic values with no observable change in the simulations. The insensitivity of the magnetic spectrum to J_6 can be understood as due to the fact that J_6 couples together parallel J_3 chains [see Fig. I(c)]. Since there is a shift between neighboring chains, a Cu^{2+} ion on one chain is coupled by J_6 to *two* Cu^{2+} ions on each neighboring chain, and since these two Cu^{2+} ions are antiparallel due to the strong antiferromagnetic J_3 interaction this coupling is frustrated for both ferromagnetic and antiferromagnetic values of J_6. As a consequence, the energy of the J_6 bonds effectively cancels. We note that the spins on neighboring chains coupled by J_6 are always perpendicular to each other in response to this frustration. It was not possible to identify a unique solution for the Hamiltonian of $BaCuTe_2O_6$ since the simulated spectrum changes only very gradually within the range of compatible solutions. Example combinations of exchange interactions that fit the data are listed in Table I.

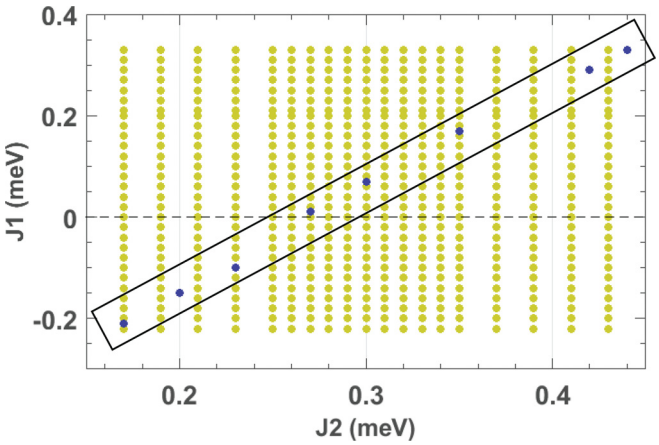

FIG. 7. Range of possible J_1 and J_2 interaction strengths in $BaCuTe_2O_6$ for $J_3 = 2.9$ meV and $J_6 = 0.035$ meV, obtained by comparing the INS data to spin-wave simulations. A large number of combinations of J_1 and J_2 were generated and tested (yellow points). Combinations lying within the black rectangular box showed good agreement with the INS spectrum, indicating the region of allowed J_1 and J_2 values. The blue points represent combinations that were investigated in particular detail.

The spin-wave spectra simulated for the solution $J_3' = \pi J_3/2$ where $J_3 = 2.90$ meV, $J_2 = 0.30$ meV, $J_1 = 0.05$ meV, and $J_6 = 0.035$ meV are shown alongside the data in the lower panels of Figs. 3–6. To make a direct comparison to the data, the simulated structure factor was convolved with a Gaussian to mimic the effects of the energy resolution and the magnetic form factor of the Cu^{2+} ion was included in the calculations. The same energy and wavevector integration ranges used for the LET data were also used in the simulations. This was achieved by averaging several simulated slices with different out-of-plane ($[K, -K, 0]$) wavevectors within the out-of-plane integration range of the data, and where appropriate a similar averaging was performed over wavevector within the in-plane integration range ($[H, H, 0]$ or $[0, 0, L]$) and over energy within the energy integration range. For the simulations of the FLEXX data, the wavevector resolution broadening was taken into account by taking the Gaussian weighted average over the expected resolution widths in the directions out-of-plane ($[K, -K, 0]$) and in-plane perpendicular to each slice by 0.1 $Å^{-1}$ and 0.02 $Å^{-1}$ respectively.

In general, good agreement between the energies and intensities of the low-energy magnetic excitations measured at $T = 2$ K and the spin-wave calculations was accomplished. The experimental data appear somewhat broader that the simulations. We attribute this to partial deconfinement of the spin waves into spinons with increasing energy.

III. DENSITY FUNCTIONAL THEORY

A. Methods

Density functional theory (DFT) provides an alternative way to determine the magnetic exchange interactions of a material based on its crystal structure. We performed all electron density functional theory calculations using the full potential local orbital (FPLO) code [30] employing the generalized gradient approximation (GGA) exchange and the correlation functional [31]. For the electronic structure calculations, we used the $T = 15$ K crystal structure of $BaCuTe_2O_6$, which was determined in Ref. [10] by neutron diffraction. For comparison we also used the $T = 80$ K crystal structure determined from x-ray diffraction [19]. The symmetry was lowered to $P2_1$ in order to have six symmetry inequivalent Cu^{2+} sites, allowing for 13 spin configurations with distinct energies, thus enabling the extraction of the exchange couplings J_1, J_2, J_3, J_4, and J_6 by energy mapping [32,33].

B. Results

Figure 8(a) shows the strengths of the exchange interactions J_1, J_2, J_3, J_4, and J_6 resulting from the DFT energy mapping for the structure determined at $T = 15$ K using powder neutron diffraction [10]. Figure 8(c) shows the same couplings, but calculated for the x-ray diffraction structure determined at $T = 80$ K [19]. Since the on-site Coulomb

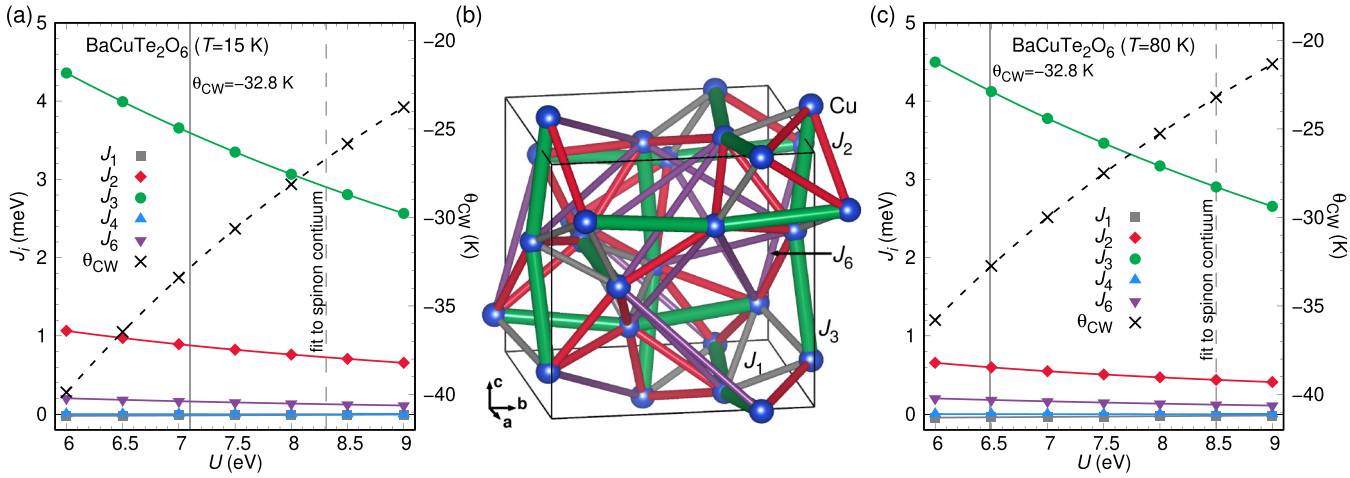

FIG. 8. (a) Exchange couplings of $BaCuTe_2O_6$ determined by DFT energy mapping for the structure determined at $T = 15$ K [10]. The solid vertical line marks the set of couplings picked out by the experimental Curie-Weiss temperature, $T_{CW} = -32.8$ K giving $U = 7.1$ eV [10]. An alternative set of interactions was obtained by using the value $J_3 = 2.90$ meV corresponding to $U = 8.3$ eV (dashed vertical line), which was extracted from the INS data. For a more detailed discussion of the choice of U see the text. (b) Network formed by the exchange interactions J_1 (grey), J_2 (red), J_3 (green), and J_6 (purple). (c) Same as (a) but calculated for the $BaCuTe_2O_6$ structure determined at $T = 80$ K [19].

repulsion U of the Cu $3d$ orbitals is unknown, the couplings were extracted for seven values of U within the expected range of 6 to 9 eV, while the Hund's rule coupling strength J_H was kept constant at 1 eV as this has been shown to describe many Cu^{2+} compounds correctly [34,35]. As there is no *a priori* way to know the U parameter, the energy mapping method needs additional information to fix the overall energy scale of the interactions. Usually, the experimental Curie-Weiss temperature is used for this purpose. We can calculate it from the exchange couplings via

$$T_{CW} = -\tfrac{2}{3}S(S+1)(J_1 + 2J_2 + J_3 + J_4 + 2J_6) \qquad (1)$$

where $S = 1/2$. The value of $T_{CW}^{\chi_{DC}} = -32.8$ K extracted from DC magnetic susceptibility measurements (χ_{DC}) for $BaCuTe_2O_6$ [10] leads to the on-site potential $U = 7.1$ eV for the $T = 15$ K crystal structure, indicated in Fig. 8(a) by the solid vertical gray line and corresponds to the set of couplings $J_1 = -0.02(1)$ meV, $J_2 = 0.88(1)$ meV, $J_3 = 3.59(1)$ meV, $J_4 = 0.00(1)$ meV, $J_6 = 0.16(1)$ meV. The same criterion for the $T = 80$ K structure [Fig. 8(c)] corresponds to $U = 6.5$ eV, yielding $J_1 = -0.04(1)$ meV, $J_2 = 0.60(1)$ meV, $J_3 = 4.13(1)$ meV, $J_4 = 0.00(1)$ meV, and $J_6 = 0.18(1)$ meV.

In the case of $BaCuTe_2O_6$, the comparison of the expression for the spinon continuum to the high-energy INS spectrum as detailed in the previous section and Ref. [10], provides another criterion for the overall energy scale by fixing the largest exchange interaction at $J_3 = 2.90$ meV. Evaluating the DFT calculation in this way leads to the Coulomb interaction $U = 8.3$ eV for the $T = 15$ K crystal structure [dashed vertical gray line in Fig. 8(a)], resulting in the set of exchange parameters $J_1 = -0.01(1)$ meV, $J_2 = 0.73(1)$ meV, $J_3 = 2.90(1)$ meV, $J_4 = 0.00(1)$ meV, and $J_6 = 0.13(1)$ meV. The energy scale of these interactions is somewhat smaller that those based on χ_{DC} and yields $T_{CW}^{INS} = -26.7$ K. The same evaluation for the $T = 80$ K structure [Fig. 8(c)] yields $U = 8.5$ eV and $J_1 = -0.02(1)$ meV, $J_2 = 0.44(1)$ meV, $J_3 = 2.90(1)$ meV, $J_4 = 0.00(1)$ meV, $J_6 = 0.12(1)$ meV and corresponds to a Curie-Weiss temperature of $T_{CW}^{INS} = -23.2$ K. This last set of couplings is in excellent agreement with the calculation reported in Ref. [19] for the same 80 K crystal structure. All these DFT results are listed for comparison in Table II. One unusual feature of the Heisenberg Hamiltonian thus obtained is the fact that the shortest exchange path ($d_{Cu-Cu} = 4.75$ Å) is found to have only a negligible exchange interaction J_1, which is less than 1% of the dominant exchange J_3. This must be due to the involved geometry of the material; the shortest superexchange paths for both couplings

TABLE II. Our DFT results based on the Curie-Weiss temperature and the J_3 value from INS for the $T = 15$ K [10] and $T = 80$ K [19] crystal structures are compared with previous DFT results [19]. Two possible sets of interactions extracted from the INS are shown for comparison, one with J_2 maximum at 0.44 meV and the other with $J_1 = 0.0$. All results are given in units of meV unless otherwise stated.

	J_1	J_2	J_3	J_4	J_6
DFT (15 K struct.) $T_{CW}^{\chi_{DC}} = -32.8$K	−0.02(1)	0.88(1)	3.59(1)	0.00(1)	0.16(1)
DFT (15 K struct.) $J_3^{INS} = 2.90$ meV	−0.01(1)	0.73(1)	2.90(1)	0.00(1)	0.13(1)
DFT (80 K struct.) $T_{CW}^{\chi_{DC}} = -32.8$K	−0.04(1)	0.60(1)	4.13(1)	0.00(1)	0.18(1)
DFT (80 K struct.) $J_3^{INS} = 2.90$ meV	−0.02(1)	0.44(1)	2.90(1)	0.00(1)	0.12(1)
DFT (80 K struct.) Ref. [19]	0	0.43	2.93	0	0.17
INS data e.g., 1: $J_2 = 0.44$ max	0.34	0.44	2.90	0.0	
INS data e.g., 2: $J_1 = 0$	0.0	0.27	2.90	0.0	

are Cu-O-Ba-O-Cu, but the path for J_1 is much more bent than the path for J_3. However, in long paths like this, complex cancellation effects, which are not accessible to simple arguments are possible.

For a given structure, the two sets of exchange interactions are very consistent despite the difference in overall energy scale. The details of the energy dispersions will be governed by the ratios J_2/J_3 and J_6/J_3. For the $T = 15$ K structure, the ratios are almost the same, being $J_2/J_3 = 24.4\%$ and $J_6/J_3 = 4.5\%$ for the interactions based on the Curie-Weiss temperature from χ_{DC}, and $J_2/J_3 = 25.0\%$ and $J_6/J_3 = 4.4\%$ for the interactions based on the INS J_3 value. The $T = 80$ K structure gives the ratios $J_2/J_3 = 14.5\%$ and $J_6/J_3 = 4.4\%$ for the $\theta_{\rm CW}$ criterion and $J_2/J_3 = 15.1\%$ and $J_6/J_3 = 4.2\%$ for the INS criterion.

IV. DISCUSSION

The Hamiltonians derived from the DFT calculations for the two different crystal structures and the INS data are in good qualitative agreement. They both show $BaCuTe_2O_6$ to be dominated by an antiferromagnetic J_3, which results in quantum spin chains running parallel to the crystallographic a, b, and c axes. The important subleading exchange is the hyperkagome interaction J_2, which couples the chains together and gives rise to long-range antiferromagnetic order. Other weaker interactions that may be present are J_1 and/or J_6.

Table II compares the DFT and INS results. Both the DFT interactions based on the Curie-Weiss temperature and on the INS J_3 value are listed. The accuracy of the value of Curie-Weiss temperature determined from the DC susceptibility data is of course important to determine the correct interactions by the first method. A significantly smaller value of $T_{\rm CW}^{\chi_{DC}} = -18.9$ K was indeed previously found [19] showing the possible range of this quantity. However, according to Figs. 8(a) and 8(c) this small $T_{\rm CW}^{\chi_{DC}}$ would imply, at $U > 9.5$ eV, values of on-site interaction U that are unusually large for Cu^{2+}. On the other hand, an accurate value of J_3 is required to determine the interactions by the second method. J_3 was found by comparing the lower boundary of the spinon continuum observed in the high-energy INS data to the des Cloiseaux-Pearson expression $(\pi \times J_3/2)|\sin(\pi H)|$ [26]. It should be noted that this expression is for an ideal chain without interchain coupling. The presence of weak interchain coupling in $BaCuTe_2O_6$ would probably reduce the renormalization factor of $(\pi/2)$ leading to an underestimation of J_3 although this effect should be small.

The choice of criterion, θ_{CW} or J_3 influences the overall scale of the interactions while maintaining the ratios of these interactions. On the other hand, the two different structures considered have somewhat different ratios of the interactions, with J_2/J_3 being larger in the case of the $T = 15$ K structure than the $T = 80$ K structure. As the exchange paths for J_2 and J_3 are complicated and the two crystal structures are very similar, no simple explanation based on perturbation theory arguments can be found. It is clear that the DFT results are highly sensitive to the structure and this underlines the importance of precise experimental determination of oxygen positions in correlated oxides. It should be noted, however, that the present DFT result for the $T = 80$ K structure are very similar to those given in Ref. [19], which also used this structure.

The fitting of the low-energy INS spectrum below $T_{\rm N}$ to spin-wave theory gives a range of possible solutions for the interchain interactions, which agree equally well with the data, where the values of J_1 and J_2 were found to be highly coupled. For $J_3 = 2.9$ meV the constraints were $0.17 < J_2 < 0.44$ meV and $2 \times J_2 - 0.56 < J_1 < 2 \times J_2 - 0.52$ meV, while a weak value of J_6 (either AFM or FM) was possible but difficult to extract from the data. Two example solutions are given in Table II. It should be noted that the excitations of frustrated magnets tend to be renormalized downward compared to spin-wave theory due to quantum fluctuations. Since the J_1 and J_2 interactions of $BaCuTe_2O_6$ are frustrated, when fitting the low-energy and low-temperature excitations to spin-wave theory, an underestimation of these interaction values could occur.

On a quantitative level, the INS results give the ratio of J_2/J_3 in the range 5.8–15.2%, which is lower than the DFT value of 25% for the $T = 15$ K structure; however, it does include the 80 K structure DFT prediction of 15%. Concerning the other interactions, DFT predicts J_1 to be close to zero while J_6 is weakly antiferromagnetic. In contrast INS finds a small but finite value of J_1 for most solutions while the value of J_6 is small and cannot be determined. There is one INS solution where J_1 is zero, which requires $J_2/J_3 = 7.5\%$—a ratio somewhat lower than the DFT predictions, which, however, can be explained by the presence of quantum fluctuations (see discussion above). On the other hand, taking the maximum allowed INS ratio of $J_2/J_3 = 15.2\%$ results in an AFM J_1 of 0.34 meV somewhat larger than the DFT prediction (see Table II).

$BaCuTe_2O_6$ can be compared to its isostructural sister compounds $SrCuTe_2O_6$ and $PbCuTe_2O_6$. While for $PbCuTe_2O_6$ the dominant antiferromagnetic J_1 and J_2 interactions lead to a highly frustrated possible spin liquid ground state, in $SrCuTe_2O_6$ the chain interaction J_3 is AFM and dominant as we find here for $BaCuTe_2O_6$. For $SrCuTe_2O_6$, $J_3 \approx 4.22$ meV [12,13,16,17,19] while the value is smaller at 2.90 meV for $BaCuTe_2O_6$ [10,19]. In $SrCuTe_2O_6$, the subleading interactions that couple the chains together and bring long-range magnetic order in the $1 \times \Gamma_1^1$ irreducible representation, are either the combination of an AFM J_1 with a weaker FM J_2 [17] or a FM J_2 and an AFM J_6 [17,19]. In contrast, for $BaCuTe_2O_6$ the long-range order forms in the $2 \times \Gamma_2^1$ irreducible representation [10], which we show here to be stabilized by an AFM J_2 interaction while weaker J_1 or J_6 interactions may also be present.

V. SUMMARY AND CONCLUSIONS

In summary, we explored the magnetic excitations of the quantum spin chain antiferromagnet $BaCuTe_2O_6$ using high-resolution INS and found that the spinon continuum at the high and medium energy ranges gives way, at low energies and temperatures, to a complex series of spin-wave modes. While the spinon continuum fixes the values of the J_3 intrachain exchange constant, a spin-wave fit taking a renormalized J_3 value into account, successfully models the low-energy spectrum. Good overall agreement was achieved for many energy

and wavevector directions, by taking into consideration the energy resolution and integration ranges. The J_2 hyperkagome exchange interaction was shown to be the subleading antiferromagnetic term responsible for coupling the chains together, and a range of allowed antiferromagnetic values was found. J_1 was shown to be weaker and highly coupled to J_2 while J_6 could not be determined.

The exchange interactions were also calculated by DFT. In agreement with INS, DFT found that J_3 is antiferromagnetic and dominant and the next strongest interaction is an antiferromagnetic J_2, a weak J_6 was also predicted while J_1 was close to zero. These calculations were surprisingly sensitive to the crystal structure so that the small difference between the structure at 80 K determined from x-ray diffraction and the 15 K structure from neutron diffraction resulted in a 40% change in the ratio of J_2/J_3. Altogether, a qualitative picture of $BaCuTe_2O_6$ emerges of a spin chain compound with frustrated antiferromagnetic hyperkagome interchain couplings, different from $SrCuTe_2O_6$ where these interactions are ferromagnetic or $PbCuTe_2O_6$, which is highly frustrated due to dominant antiferromagnetic J_1 and J_2.

In conclusion, the $ACuTe_2O_6$ family shows a strong sensitivity to the A-site ion and crystal structure, and continues to surprise us with the varied range of Hamiltonians that it harbours. We hope a deeper understanding of the structure-magnetic property relationship will be achieved in the future.

ACKNOWLEDGMENTS

We thank Jean-Sébastien Caux for his calculation of the dynamical structure factor of the spin-1/2 Heisenberg antiferromagnetic chain. B.L. acknowledges the support of Deutsche Forschungsgemeinschaft (DFG) through Project No. B06 of SFB 1143: Correlated Magnetism: From Frustration To Topology (ID 247310070). The powder synthesis, crystal growth and physical properties measurements took place at the Core Lab Quantum Materials, Helmholtz Zentrum Berlin für Materialien und Energie, Germany. We gratefully acknowledge the Science and Technology Facilities Council (STFC) for access to neutron beamtime at the LET ISIS facility and also for the provision of sample preparation.

[1] B. Koteswararao, R. Kumar, P. Khuntia, S. Bhowal, S. K. Panda, M. R. Rahman, A. V. Mahajan, I. Dasgupta, M. Baenitz, K. H. Kim, and F. C. Chou, Magnetic properties and heat capacity of the three-dimensional frustrated $S = \frac{1}{2}$ antiferromagnet $PbCuTe_2O_6$, Phys. Rev. B **90**, 035141 (2014).

[2] P. Khuntia, F. Bert, P. Mendels, B. Koteswararao, A. V. Mahajan, M. Baenitz, F. C. Chou, C. Baines, A. Amato, and Y. Furukawa, Spin Liquid State in the 3D Frustrated Antiferromagnet $PbCuTe_2O_6$: NMR and Muon Spin Relaxation Studies, Phys. Rev. Lett. **116**, 107203 (2016).

[3] S. Chillal, Y. Iqbal, H. O. Jeschke, J. A. Rodriguez-Rivera, R. Bewley, P. Manuel, D. Khalyavin, P. Steffens, R. Thomale, A. T. M. N. Islam *et al.*, Evidence for a three-dimensional quantum spin liquid in $PbCuTe_2O_6$, Nat. Commun. **11**, 2348 (2020).

[4] C. Thurn, P. Eibisch, A. Ata, U. Tutsch, Y. Saito, S. Hartmann, J. Zimmermann, A. R. N. Hanna, A. T. M. N. Islam, S. Chillal *et al.*, Spin liquid and ferroelectricity close to a quantum critical point in $PbCuTe_2O_6$, npj Quantum Mater. **6**, 95 (2021).

[5] A. R. N. Hanna, A. T. M. N. Islam, R. Feyerherm, K. Siemensmeyer, K. Karmakar, S. Chillal, and B. Lake, Crystal growth, characterization, and phase transition of $PbCuTe_2O_6$, Phys. Rev. Mater. **5**, 113401 (2021).

[6] A. H. Nakamura, K. Yoshimoto, M. Shiga, M. Nishi, and K. Kakurai, Strong antiferromagnetic spin fluctuations and the quantum spin-liquid state in geometrically frustrated β-Mn, and the transition to a spin-glass state caused by non-magnetic impurity, J. Phys.: Condens. Matter **9**, 4701 (1997).

[7] S. V. Isakov, J. M. Hopkinson, and H.-Y. Kee, Fate of partial order on trillium and distorted windmill lattices, Phys. Rev. B **78**, 014404 (2008).

[8] H.-K. Jin and Y. Zhou, Classical and quantum order in hyperkagome antiferromagnets, Phys. Rev. B **101**, 054408 (2020).

[9] L. E. Chern and Y. B. Kim, Theoretical study of quantum spin liquids in $S = \frac{1}{2}$ hyper-hyperkagome magnets: Classification, heat capacity, and dynamical spin structure factor, Phys. Rev. B **104**, 094413 (2021).

[10] A. Samartzis, S. Chillal, A. T. M. N. Islam, K. Siemensmeyer, K. Prokes, D. J. Voneshen, A. Senyshyn, D. Khalyavin, and B. Lake, Structural and magnetic properties of the quantum magnet $BaCuTe_2O_6$, Phys. Rev. B **103**, 094417 (2021).

[11] K. Momma and F. Izumi, *VESTA*: A three-dimensional visualization system for electronic and structural analysis, J. Appl. Crystallogr. **41**, 653 (2008).

[12] N. Ahmed, A. A. Tsirlin, and R. Nath, Multiple magnetic transitions in the spin-$\frac{1}{2}$ chain antiferromagnet $SrCuTe_2O_6$, Phys. Rev. B **91**, 214413 (2015).

[13] B. Koteswararao, S. K. Panda, R. Kumar, K. Yoo, A. V. Mahajan, I. Dasgupta, B. H. Chen, K. H. Kim, and F. C. Chou, Observation of S = 1/2 quasi-1D magnetic and magnetodielectric behavior in a cubic $SrCuTe_2O_6$, J. Phys.: Condens. Matter **27**, 426001 (2015).

[14] B. Koteswararao, K. Yoo, F. Chou, and K. Kim, Observation of magnetoelectric effects in a $S = 1/2$ frustrated spin chain magnet $SrCuTe_2O_6$, APL Mater. **4**, 036101 (2016).

[15] P. Saeaun, Y. Zhao, P. Piyawongwatthana, T. J. Sato, F. C. Chou, M. Avdeev, G. Gitgeatpong, and K. Matan, Magnetic properties and magnetic structure of the frustrated quasi-one-dimensional antiferromagnet $SrCuTe_2O_6$, Phys. Rev. B **102**, 134407 (2020).

[16] S. Chillal, A. T. M. N. Islam, H. Luetkens, E. Canévet, Y. Skourski, D. Khalyavin, and B. Lake, Magnetic structure of the quantum magnet $SrCuTe_2O_6$, Phys. Rev. B **102**, 224424 (2020).

[17] S. Chillal, A. T. M. N. Islam, P. Steffens, R. Bewley, and B. Lake, Weak three-dimensional coupling of Heisenberg quantum spin chains in $SrCuTe_2O_6$, Phys. Rev. B **104**, 144402 (2021).

[18] N. D. Mermin and H. Wagner, Absence of Ferromagnetism or Antiferromagnetism in One- or Two-Dimensional Isotropic Heisenberg Models, Phys. Rev. Lett. **17**, 1133 (1966).

[19] P. Bag, N. Ahmed, V. Singh, M. Sahoo, A. A. Tsirlin, and R. Nath, Low-dimensional magnetism of $BaCuTe_2O_6$, Phys. Rev. B **103**, 134410 (2021).

[20] J.-S. Caux and J. M. Maillet, Computation of Dynamical Correlation Functions of Heisenberg Chains in a Magnetic Field, Phys. Rev. Lett. **95**, 077201 (2005).

[21] R. Bewley, J. Taylor, and S. Bennington, LET, a cold neutron multi-disk chopper spectrometer at ISIS, Nucl. Instrum. Methods Phys. Res. Sect. A **637**, 128 (2011).

[22] B. Lake, A. Samartzis, E. Klyushina, N. Islam, and D. Voneshen, Investigation of a new three-dimensional frustrated quantum magnet, STFC ISIS Neutron and Muon Source, https://doi.org/10.5286/ISIS.E.RB1710246.

[23] R. Ewings, A. Buts, M. Le, J. van Duijn, I. Bustinduy, and T. Perring, Horace: Software for the analysis of data from single crystal spectroscopy experiments at time-of-flight neutron instruments, Nucl. Instrum. Methods Phys. Res. Sect. A **834**, 132 (2016).

[24] M. D. Le, M. Skoulatos, D. L. Quintero-Castro, R. Toft-Petersen, F. Groitl, K. C. Rule, and K. Habicht, The upgraded cold neutron three-axis spectrometer FLEXX at BER II at HZB, Neutron News **25**, 19 (2014).

[25] S. Toth and B. Lake, Linear spin wave theory for single-Q incommensurate magnetic structures, J. Phys.: Condens. Matter **27**, 166002 (2015).

[26] J. des Cloizeaux and J. J. Pearson, Spin-wave spectrum of the antiferromagnetic linear chain, Phys. Rev. **128**, 2131 (1962).

[27] B. Lake, D. A. Tennant, and S. E. Nagler, Novel Longitudinal Mode in the Coupled Quantum Chain Compound $KCuF_3$, Phys. Rev. Lett. **85**, 832 (2000).

[28] B. Lake, D. A. Tennant, and S. E. Nagler, Longitudinal magnetic dynamics and dimensional crossover in the quasi-one-dimensional spin-$\frac{1}{2}$ Heisenberg antiferromagnet $KCuF_3$, Phys. Rev. B **71**, 134412 (2005).

[29] B. Lake, D. A. Tennant, C. D. Frost, and S. E. Nagler, Quantum criticality and universal scaling of a quantum antiferromagnet, Nat. Mater. **4**, 329 (2005).

[30] K. Koepernik and H. Eschrig, Full-potential nonorthogonal local-orbital minimum-basis band-structure scheme, Phys. Rev. B **59**, 1743 (1999).

[31] J. P. Perdew, K. Burke, and M. Ernzerhof, Generalized Gradient Approximation Made Simple, Phys. Rev. Lett. **77**, 3865 (1996).

[32] D. Guterding, R. Valentí, and H. O. Jeschke, Reduction of magnetic interlayer coupling in barlowite through isoelectronic substitution, Phys. Rev. B **94**, 125136 (2016).

[33] Y. Iqbal, T. Müller, K. Riedl, J. Reuther, S. Rachel, R. Valentí, M. J. P. Gingras, R. Thomale, and H. O. Jeschke, Signatures of a gearwheel quantum spin liquid in a spin-$\frac{1}{2}$ pyrochlore molybdate Heisenberg antiferromagnet, Phys. Rev. Mater. **1**, 071201(R) (2017).

[34] H. O. Jeschke, F. Salvat-Pujol, and R. Valentí, First-principles determination of Heisenberg Hamiltonian parameters for the spin-$\frac{1}{2}$ kagome antiferromagnet $ZnCu_3(OH)_6Cl_2$, Phys. Rev. B **88**, 075106 (2013).

[35] H. O. Jeschke, F. Salvat-Pujol, E. Gati, N. H. Hoang, B. Wolf, M. Lang, J. A. Schlueter, and R. Valentí, Barlowite as a canted antiferromagnet: Theory and experiment, Phys. Rev. B **92**, 094417 (2015).